Probing the gravitational well: No supernova explosion in spherical symmetry with general relativistic Boltzmann neutrino transport

Matthias Liebendörfer,[1,2,3] Anthony Mezzacappa,[2] Friedrich-Karl Thielemann,[1,2] O. E. Bronson Messer,[2,3,4] W. Raphael Hix,[2,3,4] and Stephen W. Bruenn[5]

[1]*Department of Physics and Astronomy, University of Basel, Klingelbergstrasse 82, CH-4056 Basel, Switzerland*

[2]*Physics Division, Oak Ridge National Laboratory, Oak Ridge, Tennessee 37831-6354*

[3]*Department of Physics and Astronomy, University of Tennessee, Knoxville, Tennessee 37996-1200*

[4]*Joint Institute for Heavy Ion Research, Oak Ridge National Laboratory, Oak Ridge, Tennessee 37831-6374*

[5]*Department of Physics, Florida Atlantic University, Boca Raton, Florida 33431-0991*

(Received 11 December 2000; published 26 April 2001)

We report on the stellar core collapse, bounce, and postbounce evolution of a 13 $M_\odot$ star in a self-consistent general relativistic spherically symmetric simulation based on Boltzmann neutrino transport. We conclude that approximations to exact neutrino transport and the omission of general relativistic effects were not alone responsible for the failure of numerous preceding attempts to model supernova explosions in spherical symmetry. Compared to simulations in Newtonian gravity, the general relativistic simulation results in a smaller shock radius. We however argue that the higher neutrino luminosities and rms energies in the general relativistic case could lead to a larger supernova explosion energy.

DOI: 10.1103/PhysRevD.63.103004 PACS number(s): 97.60.Bw, 26.50.+x, 47.75.+f, 95.30.Jx

I. BACK TO THE PAST?

In the pioneering days of supernova simulations (Colgate and White [1], May and White [2]) the consideration of general relativity (GR) was standard. The observable event of a stellar core collapse followed by a supernova explosion was an ideal application for the newly derived Einstein equations in spherical symmetry (Misner and Sharp [3]). Lindquist [4] formulated the GR Boltzmann equation, and Wilson [5] carried out simulations based on GR Boltzmann neutrino transport using parametrized neutrino interactions. This early epoch laid the foundation leading to our current understanding of the supernova mechanism: A collapsing stellar iron core bounces at nuclear densities and launches a shock wave outwards through the infalling outer layers. The shock is energized by neutrinos diffusing out of the hot proto-neutron star, which deposit a fraction of their energy in the shock-dissociated matter via absorption on the free nucleons.

The early models underwent refinements in many respects. The equation of state evolved from simple polytropes to significantly more realistic models (Baron *et al.* [6], Lattimer and Swesty [7]). The neutrino opacities were improved (Tubbs and Schramm [8], Schinder and Shapiro [9], Bruenn [10]), and sophisticated multigroup flux-limited diffusion neutrino transport schemes were developed based on this ''standard'' nuclear physics input (Arnett [11], Bowers and Wilson [12], Bruenn [10], Myra *et al.* [13]).

However, improved approximations in the implementation of neutrino physics seemed to decrease the likelihood of successful explosions in spherical symmetry. This was especially true with the inclusion of the detailed neutrino energy spectrum via multigroup simulations and for simulations that took the inelastic neutrino–electron scattering into account (Bruenn [14,15]). The idea that the amount of dissociation energy expended by the shock ploughing through the outer iron core might be small enough to allow a prompt explosion had to be abandoned. The energy that is deposited behind the shock by the outstreaming neutrinos gained increased attention in light of a possible delayed shock revival (Wilson [16], Bethe and Wilson [17]). The amount of energy transferred, however, does not alone depend on the neutrino spectrum and luminosity of the neutrinos, but also on their angular distribution. The neutrino propagation angle determines the path length in a given radial shell; therefore, neutrinos with more tangential directions have a higher chance of absorption. A known problem with the multigroup flux-limited diffusion approximation to the Boltzmann transport equation is that, in the important semi-transparent region between the neutrinosphere and the heating region, the angular distribution of the neutrinos is not self-consistently determined by the transport equation. The consequence is an underestimation of the isotropy of the outstreaming neutrinos (Janka [18]).

The focus therefore switched on the one hand to the development of complete three-flavor Boltzmann neutrino transport (Mezzacappa and Bruenn [19–21]). In stationary comparisons between full transport and multigroup flux-limited diffusion approximations (Messer *et al.* [22], Yamada *et al.* [23]) more efficient heating was found with accurate transport. On the other hand, multidimensional phenomena were explored in the hope of finding more efficient energy transfer by neutrinos. The inclusion of neutron finger convection (see also Ref. [24]) produced explosions (Wilson and Mayle [25]) and established the delayed explosion scenario. Two-dimensional investigations of convection behind the shock and in the proto-neutron star followed with mixed results (Herant *et al.* [26], Miller *et al.* [27], Herant *et al.* [28], Burrows *et al.* [29], Janka and Müller [30], Keil *et al.* [31], Mezzacappa *et al.* [32,33]).

Semi-analytical investigations (Burrows and Goshy [34], and recently Janka [35]) illuminate the basic mechanisms, but are not able to self-consistently decide for or against

explosions nor able to predict detailed data in either of these cases.

In the search for a robust supernova mechanism, attention was directed toward simulations in the nonrelativistic (NR) limit, because explosions in GR seemed to be less likely in the selective picture that the deeper shock formation would produce larger dissociation losses and that the neutrino luminosities would suffer gravitational redshift. Multidimensional simulations that approximate general relativistic effects were performed by Fryer [36] and Fryer and Heger [37] who found reduced convection with rotating progenitors.

However, there are also beneficial GR effects: Baron *et al.* [38] reported prompt explosions in general relativity with a very soft equation of state and a leakage scheme, although these explosions were not reproduced in a general relativistic multigroup flux-limited diffusion simulation by Myra *et al.* [39] when neutrino–electron scattering was included. Swesty *et al.* [40] also did not find an explosion in a systematic investigation of realistic parameters in the equation of state. Late-time beneficial effects from the decrease in the gravitational potential by neutrino energy radiation were suggested by Goldman and Nussinov [41]. De Nisco *et al.* [42] in a quasi-static investigation pointed out that, among many detrimental effects, the hotter core in general relativistic hydrodynamics produces higher neutrino luminosities with harder spectra, resulting in a potentially beneficial impact on the heating rate. Recent dynamical simulations with GR multigroup flux-limited diffusion confirm this effect, although it does not appear to be strong enough to outweigh the negative GR contributions, i.e. the smaller heating region and greater infall velocities (Bruenn *et al.* [43]).

Recently, postbounce evolution was reexamined with Boltzmann neutrino transport without invoking multidimensional effects. As the result of an undervalued nucleon isoenergetic scattering opacity, first simulations led to an explosion of a 13 $M_\odot$ progenitor (Liebendörfer [44]). Simulations in Newtonian gravity with $O(v/c)$ Boltzmann transport and standard nuclear physics for the same progenitor do lead to an enhanced shock radius, but not to an explosion (Mezzacappa *et al.* [45]). Even with the omission of the energy loss due to the escape of μ- and τ neutrinos, independent simulations of the postbounce evolution of a 15 $M_\odot$ progenitor do not produce an explosion (Rampp and Janka [46]). The latter simulations are based on a tangent-ray method for the $O(v/c)$ Boltzmann neutrino transport (see also Burrows *et al.* [47]).

It is the purpose of this paper to report on the completion of a general relativistic radiation hydrodynamics code for spherically symmetric flows that solves the detailed Boltzmann transport equation, and to present the self-consistent simulation of stellar core collapse, bounce, and postbounce evolution for a 13 $M_\odot$ star, with all neutrino flavors and ''standard'' nuclear physics included.

II. THE RECIPE

Our simulation is initiated from the stellar precollapse model of Nomoto and Hashimoto [48]. We use the Lattimer-Swesty equation of state [7]. Simplified silicon burning is included as material from the silicon layer surrounding the iron core is instantaneously burned under energy conservation to nuclear statistical equilibrium as soon as the temperature exceeds 0.44 MeV (Mezzacappa *et al.* [45]). The simulations were carried out with a new general relativistic neutrino radiation hydrodynamics code, AGILE-BOLTZTRAN, based on a conservative formulation of GR radiation hydrodynamics in spherical symmetry and comoving coordinates (Liebendörfer *et al.* [49]).

AGILE is an implicit GR hydrodynamics code using an adaptive grid technique to conservatively implement shift vectors (Liebendörfer and Thielemann [50]). It maximizes, with respect to the number of required grid points, the resolution in regions with large density gradients and allows a smooth propagation of the shock through the outer layers [see graph (a) in Figs. 1–5]. BOLTZTRAN is an implicit three-flavor multigroup Boltzmann neutrino transport solver (Mezzacappa and Bruenn [19–21], Mezzacappa and Messer [51]) that was consistently coupled to AGILE, enabled for adaptive gridding, and extended to GR flows under omission of the small gravitational neutrino backreaction (Liebendörfer [44]). We choose 103 spatial zones, and discretize the neutrino-momentum phase space, as in Mezzacappa *et al.* [45], with 6-point Gaussian quadrature and 12 neutrino energy groups, ranging from 5 MeV to 300 MeV.

We emphasize at this point that the energy evolution in Lagrangian radiation hydrodynamics obeys the very simple conservation equation

$$\frac{\partial}{\partial t}\left[\Gamma e+\frac{2}{\Gamma+1}\left(\frac{1}{2}u^2-\frac{m}{r}\right)+\Gamma J+uH\right] + \frac{\partial}{\partial a}[4\pi r^2\alpha up+4\pi r^2\alpha\rho(uK+\Gamma H)]=0. \quad (1)$$

The variables are defined as in Lindquist [4] with the exceptions that J, H, and K represent the zeroth, first, and second angular moments of the specific radiation energy; ρ, e, and p the fluid rest mass density, internal energy, and pressure; and, a, r, and u the enclosed rest mass, the radius, and the time derivative of the radius divided by the lapse function α. The integration of Eq. (1) over the total rest mass $a_{tot}=1.55$ $M_\odot$ in the computational domain provides a check on the conservation of total energy, which can easily be monitored. Energy conservation presents a significant challenge. The cancellation of the gravitational binding energy with the internal energy sets the scale of the total energy, which is two orders of magnitude smaller than either contribution separately and comparable to the 10^{51} erg ($\sim 1\%$ of radiation energy) expected to be deposited in the heating region. Our total energy drift is no more than 5×10^{49} erg in the first 200 ms in which the explosion outcome is decided. Lepton number is conserved to within a fraction of a percent.

III. THE FAILED EXPLOSION OF A 13 $M_\odot$ STAR

We discuss the evolution of our simulation at five time slices: At bounce, and at 1 ms, 10 ms, 100 ms, and 500 ms after bounce. At each time slice we show eight graphs that

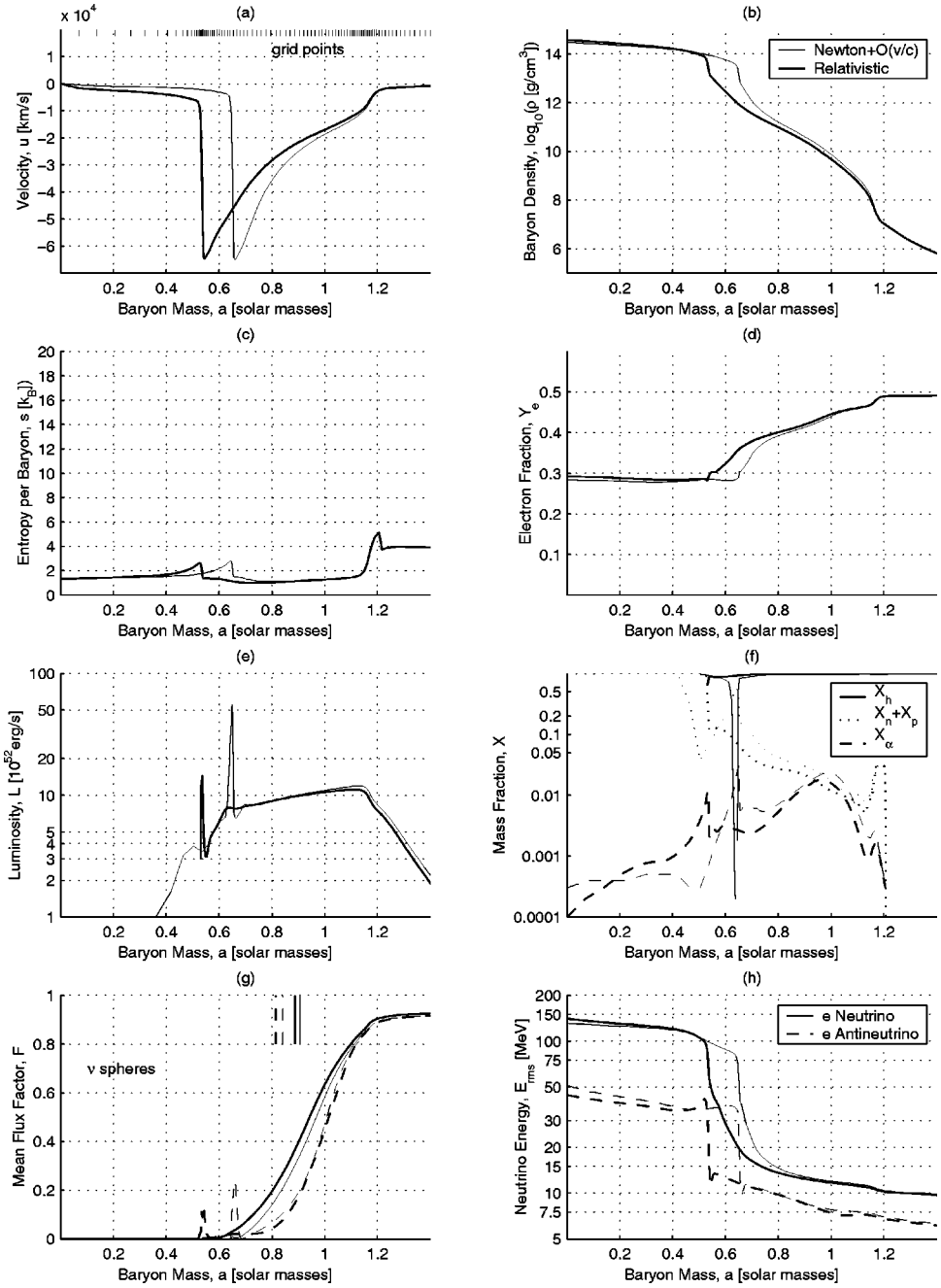

FIG. 1. Shock formation: Time slice at bounce.

compare the general relativistic evolution (GR, fat lines) to the nonrelativistic evolution (NR, thin lines). We have already reported on the NR simulation in Mezzacappa *et al.* [45]. The two runs are synchronized at bounce. The graphs are (a) the velocity profile and the location of the adaptive grid points (for the GR profiles only); (b) the rest mass density profile; (c) the entropy per baryon profile; (d) the electron fraction profile. The latter three quantities enter the equation of state and determine the composition and thermodynamic state of the local fluid element. For the convenience of interpretation, we additionally show the mass fraction of heavy nuclei, free nucleons, and alpha particles in graph (f). The remaining three graphs are devoted to neutrino radiation quantities: (e) the luminosities and (h) the rms energies defined by

$$E_{rms}=\left(\frac{\int E^2 n_\nu(E)dE}{\int n_\nu(E)dE}\right)^{1/2}. \tag{2}$$

The integrand $n_\nu(E)dE$ is the number density of neutrinos in the comoving frame energy interval $[E,E+dE]$. Graph (g) shows the mean flux factor defined by the quotient of the neutrino energy flux, H, and the neutrino energy density, J: $F\equiv H/(cJ)$. We also show the energy-averaged neutrinospheres in this plot because they separate the interior diffusion regime, with small flux factors, from the exterior regime, where large flux factors describe increasingly forward-peaked neutrino propagation through semitransparent and

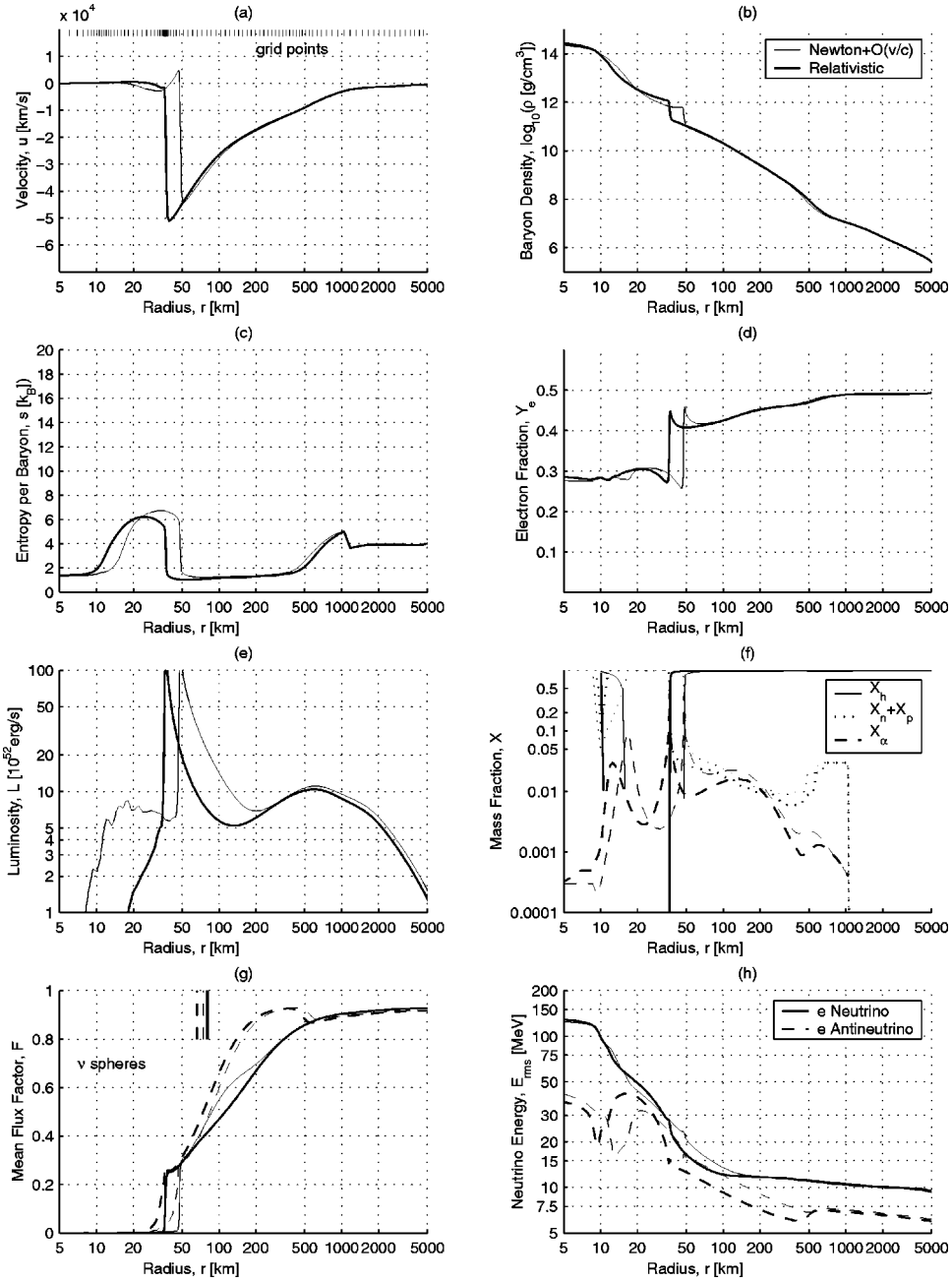

FIG. 2. Dissociation: Time slice at 1 ms after bounce.

free-streaming regions. AGILE-BOLTZTRAN solves directly for the specific neutrino distribution function, $F(t,a,E,\mu)$, at each time t. The angular resolution in the neutrino propagation angle cosine μ is set by the order of a Gaussian quadrature. This limits the representation of a strongly forward peaked radiation field, as can be observed in the mean flux factor at large radii in the graphs (g) of Fig. 1–5. However, our choice of 6-point quadrature allows an accurate representation of the mean flux factor out to a radius of at least four times the radius of the neutrinosphere. This range includes the cooling and heating region for all times in the simulation, and any influence of this numerical restriction on the dynamics is excluded. To define an energy-averaged neutrinosphere, we write the energy dependent optical depth at enclosed rest mass, a, as

$$\tau(a,E)=\int_a^{a_{tot}} \sum_i \frac{\sigma_i(E)}{4\pi r^2}\frac{n_i}{\rho}da. \tag{3}$$

The variables are defined as in Eq. (1). The index i labels different reactions, with cross sections σ_i and target number densities n_i. We draw in graph (g) the energy-averaged neutrinospheres at the location $r(a)$ where the condition

$$\frac{\int \tau(a,E)n_\nu(a,E)dE}{\int n_\nu(a,E)dE}=\frac{2}{3} \tag{4}$$

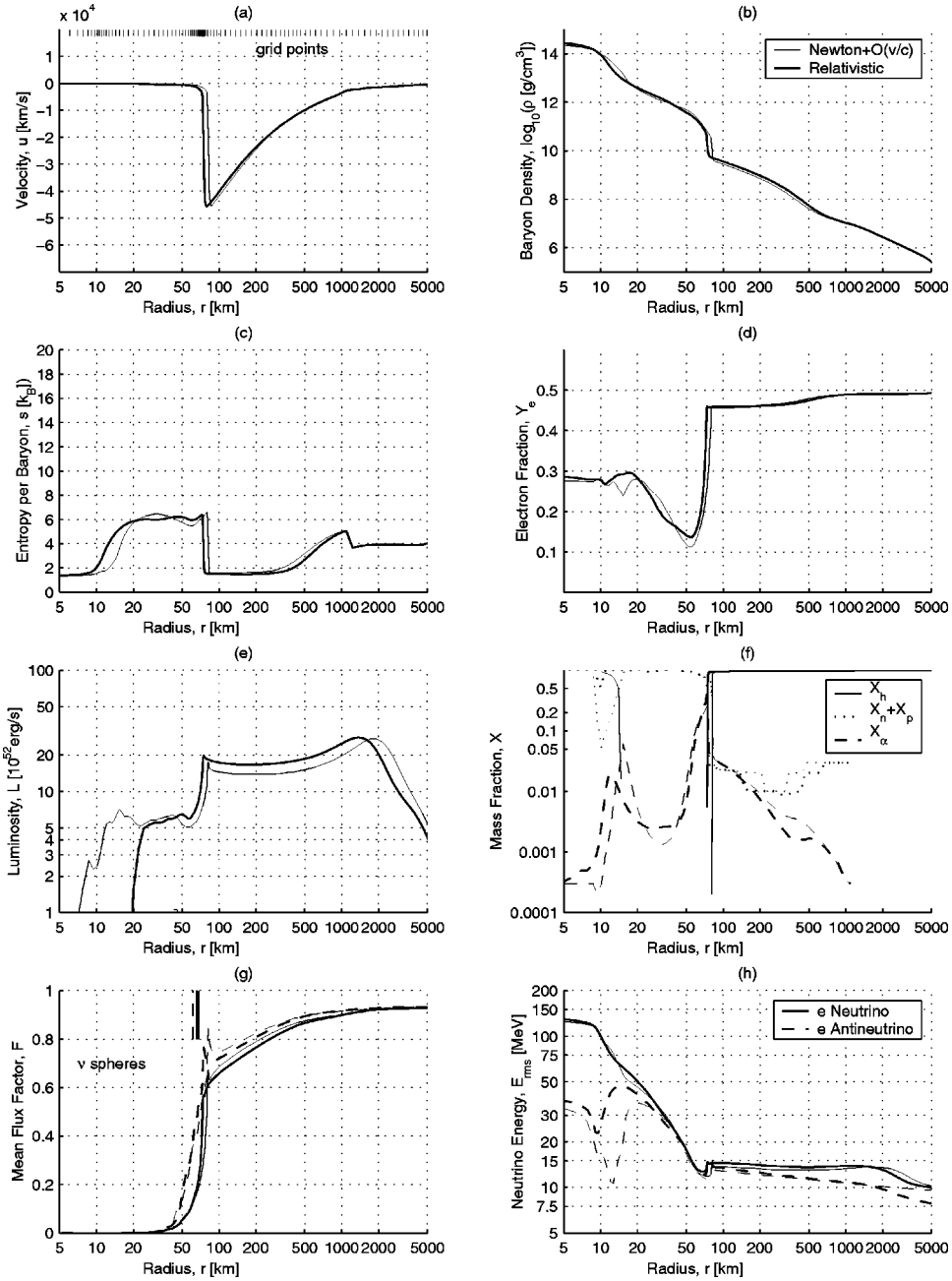

FIG. 3. Neutrino burst: Time slice at 10 ms after bounce.

for the enclosed mass a holds. The radiation quantities are given for the electron neutrino and the electron antineutrino separately. The μ and τ neutrinos do not exchange energy with the heating region. Their luminosities and rms energies are shown in later figures. In our discussion, we follow the general relativistic simulation and supply numbers for the nonrelativistic case in parentheses.

The first prominent differences between the GR and NR simulations appear at bounce in Fig. 1. At this time, the inner core passes maximum compression with a central density of 3.87×10^{14} g/cm^3 (NR: 3.05×10^{14} g/cm^3) as shown in graph (b). The homologous collapse of the causally connected inner core is abruptly halted when the central region reaches nuclear density. The short range nuclear forces suddenly increase the stiffness of the equation of state. A pressure wave emerges from the center and steepens into a shock wave at the border of the inner iron core, where it faces the disconnectedly infalling material from the outer iron core. We observe the shock formation in the velocity profile in graph (a) at an enclosed mass of 0.53 $M_\odot$ (NR: 0.65 $M_\odot$). The conversion of kinetic energy into internal energy at the shock front becomes apparent in the discontinuity of the entropy profile in graph (c). The additional discontinuity at $\sim$1.2 $M_\odot$ stems from continued silicon burning by compressional heating in the infalling material. From the composition in graph (f), we know that the shock starts to dissociate the heavy nuclei as they fall in. The shock in the NR case encloses a region of undissociated heavy nuclei at high density. The extent of this region is limited by the phase transition to bulk nuclear matter in the Lattimer-Swesty equation of state. These heavy nuclei are not present in the GR case because the shock is formed at a smaller radius, almost co-

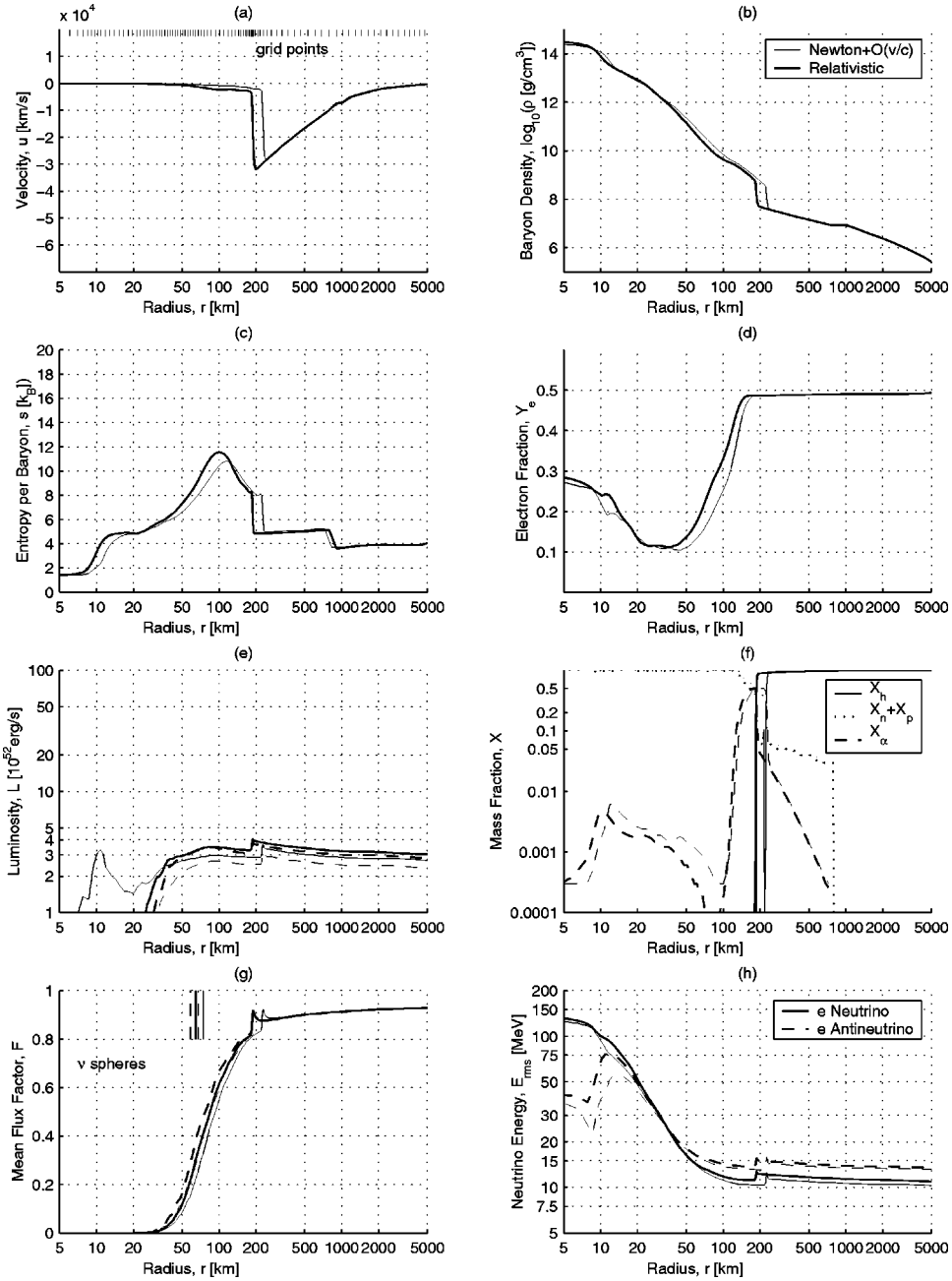

FIG. 4. Neutrino heating: Time slice at 100 ms after bounce.

incident with the location of the phase transition. The electron fraction profile in graph (d) exhibits values from 0.499 in the outer layers down to 0.29 (NR: 0.28) in the central region. The lepton fraction is set by neutrino trapping during core collapse (Sato [52], Mazurek [53]). Thereafter, smaller changes in the electron fraction are allowed according to an establishing equilibrium between electron- and neutrino-capture at constant lepton fraction (see also Mezzacappa and Bruenn [21], Messer [54]). Determined by this equilibrium are the rms energies for the electron neutrinos, as shown in graph (h). The mean flux factor in graph (g) reflects an isotropic neutrino distribution in the innermost 0.7 $M_\odot$ and outwardly directed radiation at the border of the computational domain. The peaks in the luminosity in graph (e) are caused by numerical noise at the shock front. The small flux factor in graph (g) for the electron neutrinos shows that the short range energy flux at the peak is small in the sense that it does not exceed one percent of the prevailing neutrino energy density multiplied by the velocity of light. An influence on the dynamics is therefore excluded.

One millisecond later, in Fig. 2, the shock has moved from the edge of the homologous core to densities $\sim 10^{12}$ g/cm^3 as shown in graph (b). In graph (f) we observe a region of dissociated material behind the shock. The heavy nuclei still present in the NR simulation between the shock heated matter and bulk nuclear matter have a mass of 0.15 $M_\odot$. They leave the shock an additional energy $\sim 2 \times 10^{51}$ erg with respect to the GR simulation. The NR shock in graph (a) still contains kinetic energy, while the GR shock has almost completely turned into an accretion shock. In graph (g) we see that the shock approaches the neutrinospheres. Plotted are the energy-averaged neutrinospheres lo-

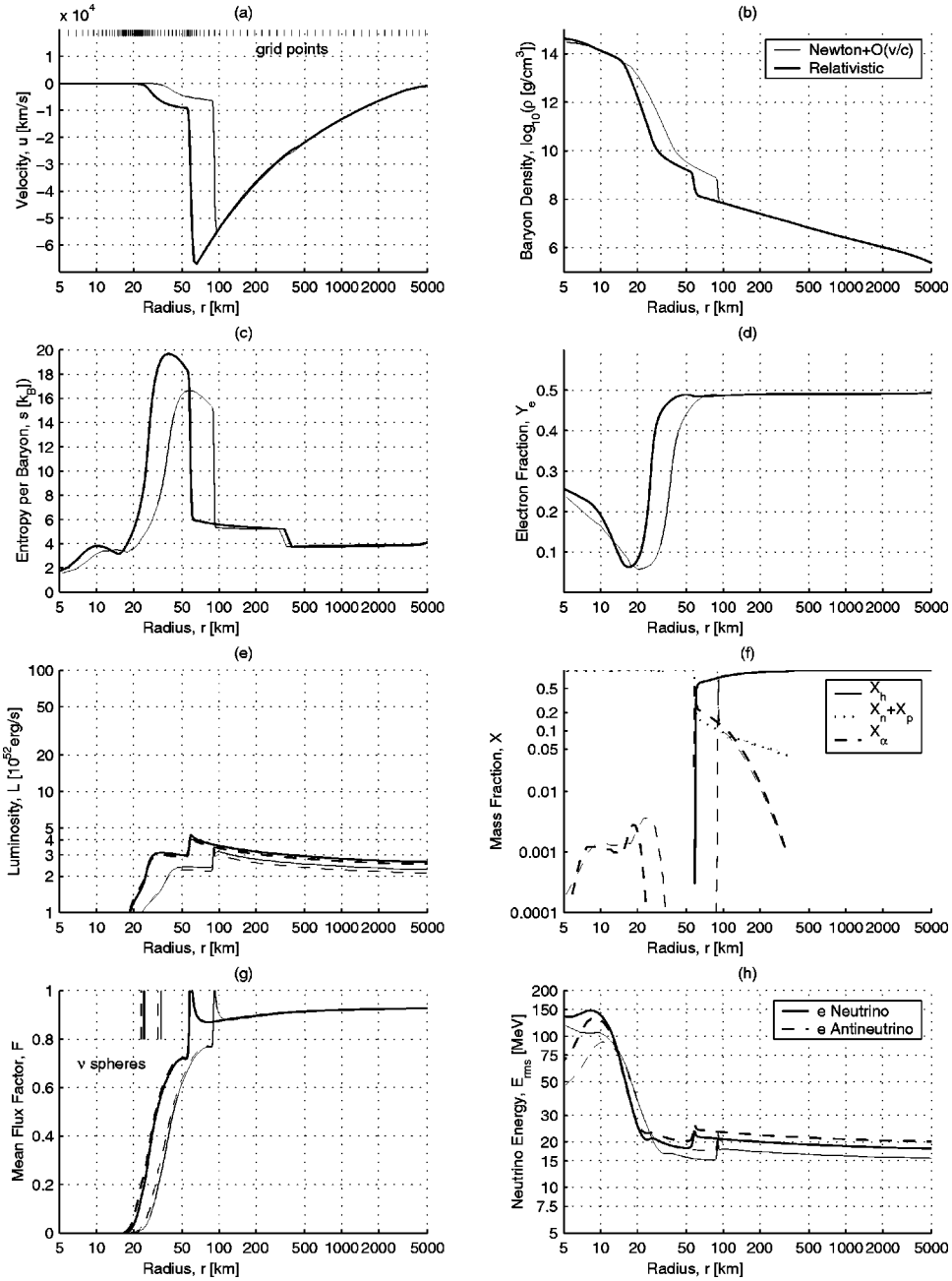

FIG. 5. Shock recession: Time slice at 500 ms after bounce.

cated in the broad region where neutrinos with different energies emanate from the diffusion regime. As the shock passes this region at about 4 ms after bounce, an energetic neutrino burst will be released from the hot shocked material, rendering it ''neutrino-visible'' to the outside world. A rise in the electron neutrino luminosity at the neutrinospheres at this time is manifest in graph (e). A dip in the rms energy profiles of the electron antineutrino in graph (h) at a radius $\sim$11 km results from the fact that there are two distinct regions producing these neutrinos: the cold compressed center of the star and the hot shocked mantle.

The time slice in Fig. 3 corresponds to 10 ms after bounce, after the launch of the neutrino burst. The luminosity peak in graph (e) has already propagated to a radius of 1800 km. This is consistent with the time of shock breakout, $t = 10$ ms - 1800 km/$c \simeq 4$ ms. The propagation of the neutrinos is also visible in their breakout rms energies. In graph (h), the neutrinos from collapse, with rms energies $\sim$10 MeV, are replaced with the burst neutrinos having an rms energy of almost 15 MeV. The electron neutrinos in the burst were produced by electron capture on free protons. The corresponding deleptonization behind the shock is dramatic in graph (d). The energy carried off with the neutrino burst completely drains the shock in both the NR and the GR cases. The pure accretion shock continues to propagate outwards as infalling material is dissociated and layered on the hot mantle [graph (a)]. This stage is the definitive end of a ''prompt,'' i.e., purely hydrodynamic, explosion.

In the standard picture, the ensuing evolution is driven by electron neutrino heating. Electron flavor neutrinos are diffusing out of the cold unshocked core as well as created in the accreting and compactifying matter around the neutrino-

spheres in a hot shocked mantle. On their escape from the semi-transparent region, they deposit energy behind the shock by absorption on free nucleons. This situation is well established at 100 ms after bounce, corresponding to Fig. 4. At this time, the accretion shock has passed the border of the original iron core. In graph (a), it has stalled at a radius of roughly 200 km. The GR shock shows a smaller stall radius than the NR shock, and the infall velocity behind the shock is about two times larger than in the NR case. The incomplete dissociation of the infalling silicon layer at the shock in graph (f) illustrates the weakening of the shock. Half of the mass remains bound in alpha particles when it crosses the shock and is dissociated later during the fall through the heating region. We additionally notice that the heavy nuclei in the cold unshocked core have either been dissociated by heating or have made the phase transition to bulk nuclear matter. Thus, the same amount of mass has been dissociated in the NR and GR cases and the corresponding earlier advantage of the NR case in the energy balance behind the shock does not persist. We see in graph (g) that the neutrino radiation becomes increasingly forward peaked outside of the neutrinospheres. There is an extended region between 50 and 200 km where the neutrinos can deposit energy by absorption. In the interior part of this region, the net cooling region, this process is more than outweighed by neutrino emission of the infalling material via electron and positron capture, as the material is compressed, heated, and layered onto the proto-neutron star. In the outer net heating region, however, electron flavor neutrino absorption just exceeds neutrino emission, leading to comparatively small net heating. The heating can indirectly be observed in graph (c) where the entropy per baryon starts to increase behind the shock. We read from graph (g) that the neutrinospheres in the more compact and hotter GR core are at smaller radii. This leads to emission of neutrinos at higher rms energies [graph (h)]. The discontinuity in the rms energies at the shock are due to the Doppler shift across it. All radiation quantities are those measured by comoving observers. This choice also leads to the luminosity step in graph (e): the infalling observer heading towards the center observes a higher luminosity than the observer almost at rest behind the shock. Although the GR luminosities in the heating region are up to 20% higher than in the NR case, the heating is not more effective in the GR case. The shocked material settles onto the proto-neutron star with a higher velocity in the deeper gravitational potential and therewith stays for a shorter time in the net heating region.

Finally, we show the situation at 500 ms after bounce in Fig. 5. The shock in graph (a) has receded to 60 km in the GR case and to 90 km in the NR case. The accretion shock, sitting deep in the gravitational potential, experiences a high ram pressure from the infalling material. All nuclei are completely dissociated when they pass the shock [graph (f)]. The infall velocities behind the shock are as large as 5000 km/s in the NR simulation and almost double that in the GR simulation. This produces high accretion luminosities in the GR case, as shown in graph (e). Higher rms energies in the GR case are evident in graph (h), as expected from the deeper position of the neutrinospheres. The net heating is not very

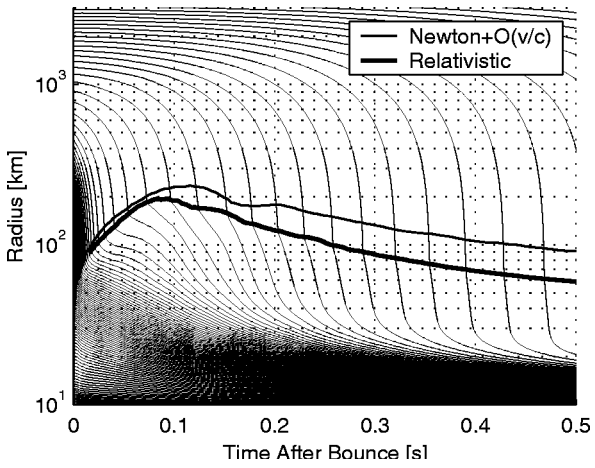

FIG. 6. Radial trajectories of equal mass shells (0.01 $M_\odot$) in the iron core and silicon layer.

efficient on the rapidly infalling material, and the entropy per baryon increases only very slowly at $\sim 1.7 k_B$/(100 ms). This rise is due to the infall of higher entropy material and the retraction of the shock radius to deeper points in the gravitational potential such that a larger kinetic energy from the infalling material is dissipated. The entropy per baryon reaches $20 k_B$ in graph (c). Overall, most features in the GR simulation are enhanced relative to the NR simulation, and the GR case exhibits a more compact structure in the proto-neutron star and its surroundings. The central density reached is 5.15×10^{14} g/cm^3 in graph (b).

The trajectories of mass shells containing 0.01 $M_\odot$ are shown for the relativistic simulation in Fig. 6. Note that the high velocities (steep gradients of mass traces) in the heating region can hardly be distinguished from the ten times larger infall velocities outside of the shock. As discussed above, mass elements are almost stopped at the shock front and do not directly fall onto the proto-neutron star surface, as might be inferred from Fig. 6. The shock position is drawn for both the GR and the NR simulation. The GR shock barely reaches 200 km, the NR shock reaches 230 km.

Graphs (a)–(d) of Fig. 7 show the neutrino heating rates (dashed lines with positive values), neutrino cooling rates (dashed lines with negative values), and their superpositions (solid lines). These energy transfer rates are shown separately for the electron neutrinos (a,b) and electron antineutrinos (c,d). We see that the net energy transfer rate is the difference between much larger cooling and heating rates, except very close to the shock, where heating clearly dominates the cooling. The location where the net heating changes sign defines the gain radius that separates the net cooling region (neutrinosphere to gain radius) from the net heating region (gain radius to shock radius). The peak net heating rate occurs rather close to the gain radius. Note the sharp cutoff at the shock in the heating by electron neutrino absorption with respect to the smoother decrease in electron antineutrino absorption. This is due to the steep drop in the free neutron mass fraction. Free neutrons are less abundant in the presence of neutron rich heavy nuclei outside the shock than the targets for electron antineutrino absorption, the free protons.

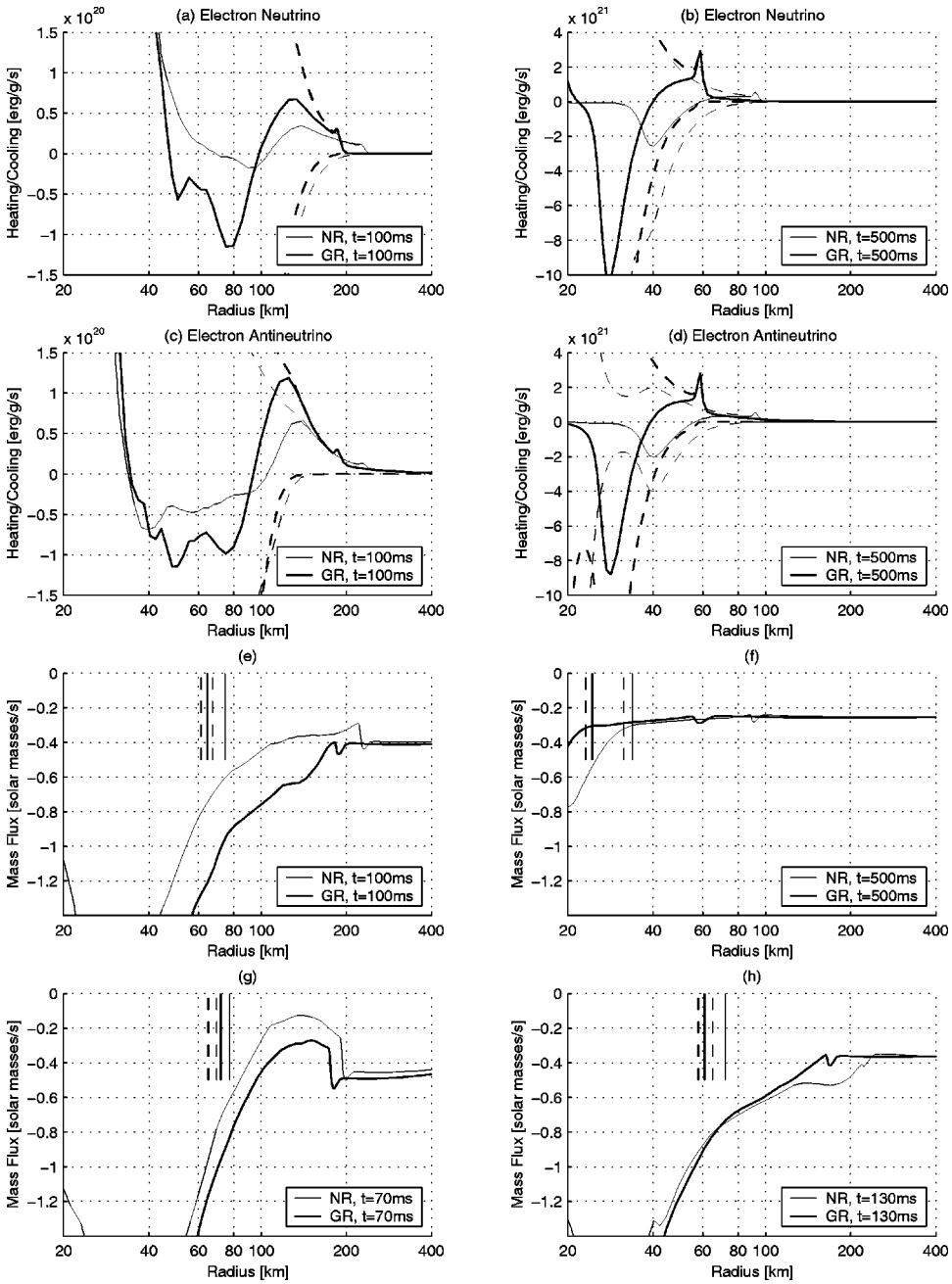

FIG. 7. Graph (a) and (b) show the energy transfer rates from emission and absorption of electron neutrinos at 100 ms and 500 ms after bounce. The dashed lines mark the separate heating and cooling rates whose superposition (solid line) leads to the net rate. Graphs (c) and (d) show the same quantities for electron antineutrino emission and absorption. Graphs (e)–(h) focus on the mass flux through spherical shells observed at constant radius. The vertical solid line shows the location of the electron neutrinosphere, the dashed line marks the electron antineutrinosphere. The four graphs correspond to times 100 ms and 500 ms, as above, and for the illustration of the time dependence, to times 70 ms and 130 ms after bounce.

At 100 ms after bounce we observe a net heating rate $\sim 10^{20}$ erg/g/s outside of the gain radius at ~ 100 km. Note that the net heating by electron antineutrino absorption is higher than the net heating by electron neutrino absorption. This is due to the fact that the increasing electron chemical potential for the infalling material, at comparable heating rates, favors cooling by electron capture compared to cooling by positron capture. This example illustrates that the net energy transfer or the net change in the electron fraction by weak interactions cannot be estimated simply based on luminosities and absorption cross sections without a detailed consideration of the compensating inverse reaction rates. We found increasing electron fractions that exceed a value of 0.5 only in our earlier exploding models where the decrease in the chemical potential in the hot expanding layers allowed for comparable electron and positron capture at a slightly favored electron neutrino absorption rate (e.g. in Ref. [44]).

Graph (e) shows the rest mass flux $4\pi r^2 u\rho/\Gamma$ through spherical surfaces measured at constant radii r at 100 ms after bounce. The time slices at 70 ms, (g), and at 130 ms, (h), are added to sketch the time dependence of the mass flux when the shock starts to recede. The largest mass flux occurs at small radii where the high-density proto-neutron star slowly adjusts its size to the newly accreted material. Most interesting for shock revival is the region between the neutrinospheres (shown as vertical bars) and the shock radius, which encloses the cooling and heating region visible in graph (a) and (b). The discontinuity in graph (g) in the mass flux at the shock front indicates that the shock is still moving outwards. The material at the gain radius and at the shock

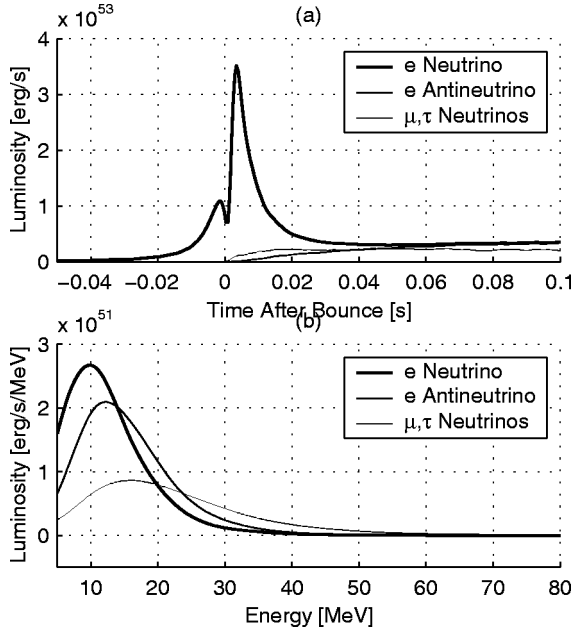

FIG. 8. (a) Neutrino luminosities before and after bounce showing the electron neutrino burst (sampled at 500 km radius and time shifted by $\Delta t = 500$ km/c). (b) Neutrino energy spectra at a radius of 500 km and 100 ms after bounce.

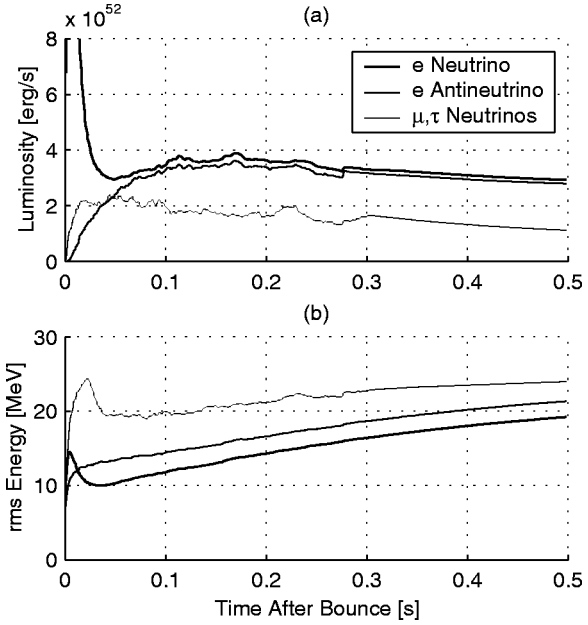

FIG. 9. Neutrino luminosities and rms energies versus time at a radius of 500 km.

radius show a comparable mass flux at 70 ms after bounce. However, at 100 ms after bounce in graph (e), and even more so at 130 ms after bounce in graph (h), a slope in the mass flux develops. The mass flux through the neutrinospheres is larger than the mass flux through the gain radius, and both are larger than the mass flux through the shock. The latter is determined by the infalling material, i.e., the density profile of the progenitor and the gravitational potential. The material in the heating region is drained from below (Janka [35]), and the conditions for heating become inefficient because of the shortened time the infalling matter spends in the heating region. In the general relativistic simulation we observe this process earlier than in the nonrelativistic simulation. The mass flux and the energy transfer rates are about a factor of two larger.

At 500 ms after bounce, the neutrinospheres and the shock have both retracted to smaller radii. The mass flux in graph (f) is almost constant down to the neutrinospheres. It is mainly set by the close to free infall of the layers around the iron core of the progenitor. Although the infall velocities have reached very large values, the actual mass flux has decreased because of the decreasing density in the outer layers. The gain radius has adjusted to a much smaller location ~ 35 km (NR ~ 60 km). In this compact configuration, the energy transfer rates have increased by more than an order of magnitude, as shown in graphs (b) and (d). At this late-time, we observe a peak in the heating rate across the shock front. Part of it is due to the increased heating rate caused by the Doppler shift in the rms energies and luminosities that applies to the material in the shock front when it is not yet completely decelerated but already dissociated. Another part is caused by numerical artifacts in the shock front: e.g., the unphysical width of the feature is set by the artificial viscosity. However, if we convolute the heating rate per mass with the density decline in the shock, we find a smooth decrease in the heating rate per volume across the shock and exclude relevant perturbations in the results owing to this feature.

We close the description of our simulations with two figures showing the temporal evolution of the GR radiation quantities. In Fig. 8 we show the neutrino luminosities at a 500 km radius as a function of time. The electron luminosity is slowly rising during collapse and decreases as the core reaches maximal density. It remains suppressed for the ~ 4 ms the shock needs to propagate to the electron neutrinosphere. The most prominent feature is the electron neutrino burst, reaching 3.5×10^{53} erg/s at shock breakout, and declining afterwards. Graph (b) shows the luminosity spectra at 100 ms after bounce, just before the shock starts to recede. Figure (9) shows the long-term evolution with better resolution, sampled at a radius of 500 km. The maximum luminosities in the GR simulation are 3.9×10^{52} erg/s, 3.6×10^{52} erg/s, and 2.3×10^{52} erg/s for the electron neutrino, electron antineutrino, and μ and τ neutrinos respectively. This is roughly 10% more than the maximum luminosities reached (at different times) in the NR simulation. The GR results also show higher rms energies, but no qualitatively different features.

IV. CONCLUSION AND OUTLOOK

We have completed the construction of a general relativistic radiation hydrodynamics code, AGILE-BOLTZTRAN, and simulated the spherically symmetric, general relativistic

core collapse, bounce, and postbounce evolution of a 13 $M_\odot$ progenitor. We investigate the confluence of (i) matter and radiation in a deeper effective gravitational potential, (ii) a GR core hydrodynamic structure that acts as a more intense neutrino source, and (iii) an increased heating efficiency obtained from accurate three-flavor Boltzmann neutrino transport. However, we find that the combination of these ingredients does not result in a supernova explosion. Our model shares this outcome with recent simulations that investigated a subset of these issues (Rampp and Janka [46], Mezzacappa *et al.* [45], Bruenn *et al.* [43]).

(i) During core collapse, the homologous core is smaller in the general relativistic gravitational potential than in Newtonian gravity. This leads to a smaller enclosed mass at shock formation and higher initial dissociation losses when the shock moves to larger radii. The neutrinos in curved spacetime propagate on trajectories with nearly constant $\varepsilon = (\Gamma + u\mu)E$ and $b = r\sqrt{1-\mu^2}/(\Gamma + u\mu)$, where μ and E are the neutrino propagation-angle cosine and energy measured by comoving observers. This latter effect is of little importance for our low-mass progenitor. The GR corrections for redshift and curvature between the neutrinospheres and the heating region do not exceed 3% until shock recession, and increase only later, when the neutrinospheres have receded to smaller radii. (ii) Nonlinear effects in GR enhance the self-gravitation in the high-density domain of the proto-neutron star. The latter becomes more compact and exhibits higher internal energies. This in turn leads to higher core and accretion luminosities with harder spectra in all neutrino flavors (Bruenn *et al.* [43]). (iii) The solution of the Boltzmann equation for the neutrino transport reproduces accurately the angular distribution of the neutrino radiation field behind the shock. An increased angular spread in the semi-transparent regime keeps the outstreaming neutrinos longer in the heating region and, therefore, increases the absorption efficiency with respect to the multigroup flux-limited diffusion approximation (Messer *et al.* [22], Yamada *et al.* [23]).

The main difference between the GR and NR simulations stems from the difference in the size of the proto-neutron star, which is caused by the nonlinear GR effects at very high densities in the center of the star. At radii of order 100 km and larger, the gravitational potential becomes comparable in the GR and NR cases. However, large differences arise if the steep gravitational well is probed at different *positions* in the GR and NR simulations, as happens with accretion down to the neutrinospheres, which represent the outer ''boundary'' of the proto-neutron star. The deeper neutrinospheres in the more compact GR case receive material that has traversed a larger potential difference and, settling deeper in the well, produces more energetic accretion luminosities. After the shock has stalled, the surrounding layers (cooling-heating region, shock radius) adjust to a smaller radius and settle to a stationary equilibrium in the spirit of Burrows and Goshy [34]. In the GR simulation, this occurs at a smaller radius, deeper in the gravitational well, with higher infall velocities, higher accretion luminosities, and higher heating rates, which sustain equilibrium between the pressure behind the shock and the increased ram pressure ahead of it. The tight feedback between infall velocity, accretion luminosity and heating leads to *higher* luminosities in more compact configurations where the shock stalls at a *smaller* radius. Moreover, this self regulation has observable consequences: The gravitational well is probed when the proto-neutron star radius is set, tuning the directly observable neutrino luminosities and spectra.

From the comparison between the NR and GR shock trajectories in Fig. 6, we might be tempted to conclude that the chances for a vigorous explosion in the more realistic GR case are more pessimistic than in the NR case. We however feel that such a conclusion would be premature if only based on a postbounce evolution that fails to reproduce an explosion. An actual boost in the explosion energy due to general relativistic effects has been seen by Liebendörfer [44] in a simulation that led to an explosion because of incorrect nucleon isoenergetic scattering opacities. As in the simulation with the correct opacities, a more compact proto-neutron star was created and higher luminosities with harder spectra developed in the GR case. However, in the exploding case, a turning point occurred where the infall velocities behind the shock almost vanished. This happened $\sim$100 ms after bounce, before the heating region had the time to step deeper into the gravitational well. The consequence was a more efficient heating with the GR enhanced luminosities and spectra, which lead to a more energetic supernova than in the corresponding NR simulation. Our conclusion for low-mass progenitors with small redshifts is: GR effects do not cause explosions in our current simulations. An essential physical ingredient is missing. However, GR effects may eventually drive an explosion more efficiently when it has been launched.

There are many facets of a supernova that cannot consistently be included in a spherically symmetric model. There is no doubt that convection behind the shock will occur, and significant rotation and strong magnetic fields might be present. Observations of neutron star kicks, mixing of species, inhomogeneous ejecta, and polarization of spectra suggest the presence of asymmetries in supernova explosions (e.g. Tueller *et al.* [55], Strom *et al.* [56], Galama *et al.* [57], Leonard *et al.* [58], and references therein). Motivated by such observations, various multi-dimensional explosion mechanisms have been explored (Herant *et al.* [26], Miller *et al.* [27], Herant *et al.* [28], Burrows *et al.* [29], Janka and Müller [30], Mezzacappa *et al.* [33], Fryer [36], Fryer and Heger [37]) and jet-based explosion scenarios received new momentum (Höflich *et al.* [59], Khokhlov *et al.* [60], MacFadyen and Woosley [61], Wheeler *et al.* [62]). It remains a challenge for the next decade to include all relevant physics in supernova simulations in an attempt to reproduce supernova observations in detail. For the time being, one has to single out a subset of the known physics and to investigate the role each part plays in the restricted simulation. It is natural to start with ingredients that have long been believed to be essential for the explosion and to add modifiers in a systematic way until the observables can be reproduced (Mezzacappa *et al.* [45]). Spherically symmetric supernova modeling has a long tradition and is nearing a definitive point in the sense that high-resolution hydrodynamics, general relativity, complete Boltzmann neutrino transport, and reasonable nuclear and weak interaction physics are being

combined to dispel remaining uncertainties. Models that are restricted to spherical symmetry allow the detailed simulation and study of radiation hydrodynamic flows in general relativity, with all feedbacks included. Moreover, they will provide a gauge for unavoidable approximations in future, more inclusive simulations. The accurate description of the high-density region in the proto-neutron star and realistic multigroup transport are prerequisites for the evaluation of new developments in the input physics. With the former well underway, research in spherically symmetric supernova models can focus on the uncertainties in the nuclear physics and neutrino interactions. A major revision in the equation of state (Shen *et al.* [63]; see also Swesty *et al.* [40]) or in the neutrino-matter interactions (Burrows and Sawyer [64], Reddy *et al.* [65], Thompson *et al.* [66], Langanke and Martinez-Pinedo [67]), or the inclusion of neutrino oscillations (Fuller *et al.* [68], Abazajian *et al.* [69]), might be the last opportunity to understand the most basic supernova observable in restricted spherical models: explosion.

ACKNOWLEDGMENTS

We enjoyed fruitful discussions with Thomas Janka and Markus Rampp. M.L. is supported by the National Science Foundation under contract AST-9877130 and, formerly, was supported by the Swiss National Science Foundation under contract 20-53798.98. A.M. is supported at the Oak Ridge National Laboratory, managed by UT-Battelle, LLC, for the U.S. Department of Energy under contract DE-AC05-00OR22725. F.-K.T. is supported in part by the Swiss National Science Foundation under contract 20-61822.00 and the Oak Ridge National Laboratory. O.E.B.M. is supported by funds from the Joint Institute for Heavy Ion Research and a Dept. of Energy PECASE Grant. W.R.H. is supported by NASA under contract NAG5-8405, by funds from the Joint Institute for Heavy Ion Research and a Department of Energy PECASE Grant. S.W.B. is supported by the NSF under contract 96-18423 and by NASA under contract NAG5-3903. Our simulations were carried out on the ORNL Physics Division Cray J90 and the National Energy Research Supercomputer Center Cray J90.

[1] S. A. Colgate and R. H. White, Astrophys. J. **143**, 626 (1966).
[2] M. M. May and R. H. White, Comput. Phys. **7**, 219 (1967).
[3] C. W. Misner and D. H. Sharp, Phys. Rev. **136**, B571 (1964).
[4] R. W. Lindquist, Ann. Phys. (N.Y.) **37**, 487 (1966).
[5] J. R. Wilson, Astrophys. J. **163**, 209 (1971).
[6] E. Baron, J. Cooperstein, and S. Kahana, Nucl. Phys. **A440**, 744 (1985).
[7] J. Lattimer and F. D. Swesty, Nucl. Phys. **A535**, 331 (1991).
[8] D. Tubbs and D. Schramm, Astrophys. J. **201**, 467 (1975).
[9] P. J. Schinder and S. L. Shapiro, Astrophys. J., Suppl. Ser. **50**, 23 (1982).
[10] S. W. Bruenn, Astrophys. J., Suppl. Ser. **58**, 771 (1985).
[11] W. D. Arnett, Astrophys. J. **218**, 815 (1977).
[12] R. L. Bowers and J. R. Wilson, Astrophys. J., Suppl. Ser. **50**, 115 (1982).
[13] E. S. Myra, S. A. Bludman, Y. Hoffman, I. Lichtenstadt, N. Sack, and K. A. Van Riper, Astrophys. J. **318**, 744 (1987).
[14] S. W. Bruenn, Astrophys. J. **340**, 955 (1989).
[15] S. W. Bruenn, Astrophys. J. **341**, 385 (1989).
[16] J. R. Wilson, in *Numerical Astrophysics*, edited by J. M. Centrella, J. M. LeBlanc, and R. L. Bowers (Jones and Bartlett, Boston, 1985).
[17] H. A. Bethe and J. R. Wilson, Astrophys. J. **295**, 14 (1985).
[18] H.-T. Janka, Astron. Astrophys. **256**, 452 (1992).
[19] A. Mezzacappa and S. W. Bruenn, Astrophys. J. **405**, 669 (1993).
[20] A. Mezzacappa and S. W. Bruenn, Astrophys. J. **405**, 637 (1993).
[21] A. Mezzacappa and S. W. Bruenn, Astrophys. J. **410**, 740 (1993).
[22] O. E. B. Messer, A. Mezzacappa, S. W. Bruenn, and M. W. Guidry, Astrophys. J. **507**, 353 (1998).
[23] S. Yamada, H.-T. Janka, and H. Suzuki, Astron. Astrophys. **344**, 533 (1999).
[24] S. W. Bruenn and T. Dineva, Astrophys. J. Lett. **458**, L71 (1996).
[25] J. R. Wilson and R. W. Mayle, Phys. Rep. **227**, 97 (1993).
[26] M. Herant, W. Benz, and S. A. Colgate, Astrophys. J. **395**, 642 (1992).
[27] D. S. Miller, J. R. Wilson, and R. W. Mayle, Astrophys. J. **415**, 278 (1993).
[28] M. Herant, W. Benz, R. W. Hix, C. L. Fryer, and S. A. Colgate, Astrophys. J. **435**, 339 (1994).
[29] A. Burrows, J. Mayes, and B. A. Fryxell, Astrophys. J. **450**, 830 (1995).
[30] H.-T. Janka and E. Müller, Astron. Astrophys. **306**, 167 (1996).
[31] W. Keil, H.-T. Janka, and E. Müller, Astrophys. J. Lett. **473**, L111 (1996).
[32] A. Mezzacappa, A. C. Calder, S. W. Bruenn, J. M. Blondin, M. W. Guidry, M. R. Strayer, and A. S. Umar, Astrophys. J. **493**, 848 (1998).
[33] A. Mezzacappa, A. C. Calder, S. W. Bruenn, J. M. Blondin, M. W. Guidry, M. R. Strayer, and A. S. Umar, Astrophys. J. **495**, 911 (1998).
[34] A. Burrows and J. Goshy, Astrophys. J. Lett. **416**, L75 (1993).
[35] H.-T. Janka, Astron. Astrophys. (to be published), astro-ph/0008432.
[36] C. F. Fryer, Astrophys. J. **522**, 413 (1999).
[37] C. F. Fryer and A. Heger, Astrophys. J. **541**, 1033 (2000).
[38] E. Baron, J. Cooperstein, and S. Kahana, Phys. Rev. Lett. **55**, 126 (1985).
[39] E. S. Myra and S. A. Bludman, Astrophys. J. **340**, 384 (1989).
[40] E. D. Swesty, J. M. Lattimer, and E. S. Myra, Astrophys. J. **425**, 195 (1994).
[41] I. Goldman and S. Nussinov, Astrophys. J. **403**, 706 (1993).
[42] K. De Nisco, S. W. Bruenn, and A. Mezzacappa, Bulletin of the 191st American Astronomical Society Meeting, Washing-

ton, D.C., 1998, edited by R. W. Milkey (AAS, Washington, 1997), Vol. 29, p. 39.10.
[43] S. W. Bruenn, K. R. DeNisco, and A. Mezzacappa, Astrophys. J. (to be published), astro-ph/0101400.
[44] M. Liebendörfer, Ph.D. thesis, University of Basel, Basel, Switzerland, 2000.
[45] A. Mezzacappa, M. Liebendörder, O. E. B. Messer, R. W. Hix, F.-K. Thielemann, and S. W. Bruenn, Phys. Rev. Lett. **86**, 1935 (2001).
[46] M. Rampp and H.-T. Janka, Astrophys. J. Lett. **539**, L33 (2000).
[47] A. Burrows, T. Young, Ph. Pinto, R. Eastman, and T. A. Thompson, Astrophys. J. **539**, 865 (2000).
[48] K. Nomoto and M. Hashimoto, Phys. Rep. **163**, 13 (1988).
[49] M. Liebendörfer, A. Mezzacappa, and F.-K. Thielemann, Phys. Rev. D **63**, 104003 (2001).
[50] M. Liebendörfer and F.-K. Thielemann, in *Nineteenth Texas Symposium on Relativistic Astrophysics*, edited by E. Aubourg, T. Montmerle, J. Paul, and P. Peter (Elsevier Science B.V., Amsterdam, 2000).
[51] A. Mezzacappa and O. E. B. Messer, J. Comput. Appl. Math. **109**, 281 (1999).
[52] K. Sato, Prog. Theor. Phys. **53**, 595 (1975); **54**, 1325 (1975).
[53] T. Mazurek, Astrophys. J. Lett. **207**, L87 (1976).
[54] O. E. B. Messer, Ph.D. thesis, University of Tennessee, Knoxville, 2000.
[55] J. Tueller, S. Barthelmy, N. Gehrels, M. Leventhal, C. J. MacCallum, and B. J. Teegarden, in *Supernovae*, edited by S. E. Woosley (Springer, Berlin, 1991), p. 278.
[56] R. Strom, H. M. Johnston, F. Verbunt, and B. Aschenbach, Nature (London) **373**, 587 (1995).
[57] T. J. Galama, P. M. Vreeswijk, J. van Paradijs, C. Kouveliotou, T. Augusteijn, O. R. Hainaut, F. Patat, H. Boehnhardt, J. Brewer, V. Doublier, J.-F. Gonzalez, C. Lidman, B. Leibundgut, J. Heise, J. in 't Zand, P. J. Groot, R. G. Strom, P. Mazzali, K. Iwamoto, K. Nomoto, H. Umeda, T. Nakamura, T. Koshut, M. Kippen, C. Robinson, P. de Wildt, R. A. M. J. Wijers, N. Tanvir, J. Greiner, E. Pian, E. Palazzi, F. Frontera, N. Masetti, L. Nicastro, E. Malozzi, M. Feroci, E. Costa, L. Piro, B. A. Peterson, C. Tinney, B. Boyle, R. Cannon, R. Stathakis, M. C. Begam, and P. Ianna, Nature (London) **395**, 670 (1998).
[58] D. C. Leonard, A. V. Filippenko, A. J. Barth, and T. Matheson, Astrophys. J. **536**, 239 (2000).
[59] P. Höflich, J. C. Wheeler, and L. Wang, Astrophys. J. **521**, 179 (1999).
[60] A. M. Khokhlov, P. A. Höflich, E. S. Oran, J. C. Wheeler, L. Wang, and A. Yu. Chtchelkanova, Astrophys. J. Lett. **524**, L107 (1999).
[61] A. I. MacFadyen and S. E. Woosley, Astrophys. J. **524**, 262 (1999).
[62] J. C. Wheeler, I. Yi, P. Höflich, and L. Wang, Astrophys. J. **537**, 810 (2000).
[63] H. Shen, H. Toki, K. Oyamatsu, and K. Sumiyoshi, Nucl. Phys. **A637**, 435 (1998).
[64] A. Burrows and R. F. Sawyer, Phys. Rev. C **58**, 554 (1998).
[65] S. Reddy, M. Prakash, J. M. Lattimer, and J. A. Pons, Phys. Rev. C **59**, 2888 (1999).
[66] T. A. Thompson, A. Burrows, and J. E. Horvath, Phys. Rev. C **62**, 035802 (2000).
[67] K. H. Langanke and G. Martinez-Pinedo, Nucl. Phys. **A673**, 481 (2000).
[68] G. M. Fuller, R. W. Mayle, B. S. Meyer, and J. R. Wilson, Astrophys. J. **389**, 517 (1992).
[69] K. Abazajian, G. M. Fuller, and M. Patel, astro-ph/0101524.